The high partial wave phenomenon of spin changing atomic transitions

BERRINGTON, K. A.

Published version

BERRINGTON, K. A. (2006). The high partial wave phenomenon of spin changing atomic transitions. Journal of physics B: Atomic, molecular and optical physics, 39, 3873-3887.

The high partial wave phenomenon of spin changing atomic transitions

K A Berrington
City Campus, Sheffield Hallam University, Sheffield, S1 1WB, UK
E-mail: k.berrington@shu.ac.uk

Submitted: July 14, 2006

Abstract

The collisional transition between two highly excited atomic states with different spin is investigated theoretically. Taking helium-like $n^1S - n^3P$ as an example, it is found that the transition is driven in the highly ionized Fe ion purely by exchange, and the cross section becomes increasingly dominated by partial waves of high orbital angular momentum as the scattering energy increases. Whereas for the near-neutral Li ion the transition is dominated by channel coupling in low partial waves. Analytical benchmarks and numerical methods are developed for the accurate calculation of the exchange integral at high angular momentum. It is shown how the partial wave and energy dependence of the collision strength for high n spin changing transitions in the highly ionized ion is related to the overlap of the extended atomic orbitals.

1 Introduction

Spin changing transitions caused by electron impact are very important in atomic physics, providing a mechanism for populating the different spin states of an ionized plasma, for example. At least three electrons are involved (two atomic electrons and the incident one), and the process is a manifestation of angular momentum coupling, antisymmetrization and the electron-electron interaction, making this an interesting problem in its own right.

The calculation of excitation cross sections for transitions involving states of atoms and ions is a well developed area of modern atomic physics, with powerful computer codes able to handle many hundreds of atomic states, and with a wide range of laboratory and astrophysical applications providing stimulation for further development. For example, codes based on the R-matrix method (Burke and Berrington 1993) are used in large scale international collaborations such as

the Iron Project to calculate Fe ion rates for astrophysics (Hummer et al 1993) and the RmaX network to calculate data for X-ray transitions (RmaX 2006, Norrington 2006), and are widely used by many people for diverse applications.

A feature of such calculations is the partial wave expansion, where a calculation with full exchange is taken to a reasonably high orbital angular momentum (typically J or $L = 20$, depending on the coupling scheme adopted), and then a 'top-up' based on a no-exchange calculation or a Coulomb-Bethe approximation is used to complete the partial sum to obtain the total cross section (Burgess 1974, Burgess et al 1970). In addition, many forbidden transitions are either fully converged at low partial waves, or can be summed to reasonable accuracy by assuming a geometric progression in angular momentum.

However, the calculation of spin changing cross sections particularly for high n states presents a problem which has so far not been addressed. Examples will be shown of such cross sections being dominated by high partial wave contributions.

It should be emphasised that the present work may not have much practical significance in applications: in all cases considered the cross sections are very small. Instead, the present paper should be seen as an attempt to examine the physics and the numerical implications of this high partial wave phenomenon.

In the subsection below we briefly describe the equations of scattering theory relevant to the subject matter of this paper. Section 2 identifies problems with existing procedures for the exchange R_k integral for high k, and in section 3 we develop analytical solutions which we use to benchmark numerical methods. Section 4 describes an application to He-like ions, focusing on the behaviour of the $n^1S - n^3P$ partial collision strength, and in section 5 we discuss the high partial wave mechanism of spin changing transitions, before concluding in section 6.

1.1 Theoretical background

Electron scattering cross sections can be computed by solving quantum mechanical equations for the wavefunction Ψ. In the time independent formalism for a target system of N electrons and one incident electron of total energy E,

$$H^{N+1}\Psi = E\Psi. \tag{1}$$

The Hamiltonian H^{N+1} consists of kinetic energy and relativistic operators and the Coulomb interaction between charged particles. For atomic systems, solutions Ψ of (1) can be constructed as products of one-electron functions in spherical polar coordinates. Antisymmetrization ensures that electron exchange is taken into account in the Coulomb repulsion terms between pairs of electrons, $\sum_{n=1}^{N+1}\sum_{m>n}^{N+1} e^2/|\boldsymbol{r}_n - \boldsymbol{r}_m|$, where $\boldsymbol{r}_i$ are the radial vectors of each electron.

We can solve (1) variationally in a basis which allows for configuration interaction and target state close-coupling with the continuum. This involves setting up and diagonalizing a Hamiltonian matrix in the basis, with matrix elements

of H^{N+1} requiring integrations over all electronic coordinates. In the matrix elements arising from the two-electron terms which concern us in this paper, the spin and orbital angular momenta, which are tied together only by antisymmetrization and angular momentum addition, are separated by fractional parentage expansions (Fano 1965), and the angular and radial integrals become separable by expanding in terms of spherical harmonics:

$$\frac{1}{|\boldsymbol{r}_n - \boldsymbol{r}_m|} = \sum_{k\mu} \frac{4\pi}{2k+1} Y_k^\mu(\hat{r}_n) Y_k^\mu(\hat{r}_m) V_k(r_n, r_m), \quad V_k(r,s) = \frac{\min(r,s)^k}{\max(r,s)^{k+1}} \qquad (2)$$

The two-electron radial integral then involves four radial orbitals U_i, two on each side of the operator:

$$R^k_{1234} = \int_0^\infty \mathrm{d}s \int_0^\infty \mathrm{d}r\; U_1(r) U_2(s) V_k(r,s) U_3(r) U_4(s) = \int_0^\infty \mathrm{d}s\; U_2(s)\, y^k_{13}(s)\, U_4(s), \quad (3)$$

with the multipole potential functions given by

$$y^k_{13}(s) = \frac{1}{s^{k+1}} \int_0^s \mathrm{d}r\; U_1(r) r^k\, U_3(r) + s^k \int_s^a \mathrm{d}r\; U_1(r) \frac{1}{r^{k+1}}\, U_3(r) \qquad (4)$$

With only one scattering electron, there will be least one bound orbital on each side of the matrix element which exponentially decays with r, so the infinity limits of (3) can be replaced by finite limits ($r = a$) as shown in (4), and this feature is exploited particularly in R-matrix theory.

2 Statement of the problem

Difficulties arise in evaluating the two-electron continuum-continuum exchange integral for high partial waves, typically for angular momenta $\gg 20$.

Continuum-continuum integrals have a bound and a continuum orbital on each side of the two-electron operator in (3). The orthogonality of spherical harmonics restricts the range of k:

$$|l_1 - l_3| \le k \le l_1 + l_3, \qquad |l_2 - l_4| \le k \le l_2 + l_4. \qquad (5)$$

In the direct integral (bound,continuum; bound,continuum), U_1 and U_3 are bound orbitals and generally have low orbital angular momenta. The range of k is therefore over low values and there is no particular problem carrying out the integrals. However, in the exchange integral (bound,continuum; continuum,bound), U_2 and U_3 are continuum orbitals with potentially large angular momenta, so leading to large values of k. The resulting large powers of r in the integrations of (4) require careful analytical techniques, as described in the next section.

In many applications, orbitals and integrations are numerical on a radial mesh. In particular, the widely used R-matrix codes DARC (Ait-Tahar et al 1996; Norrington 2006) and RMATRX1 (Berrington et al 1995; RmaX 2006) both use

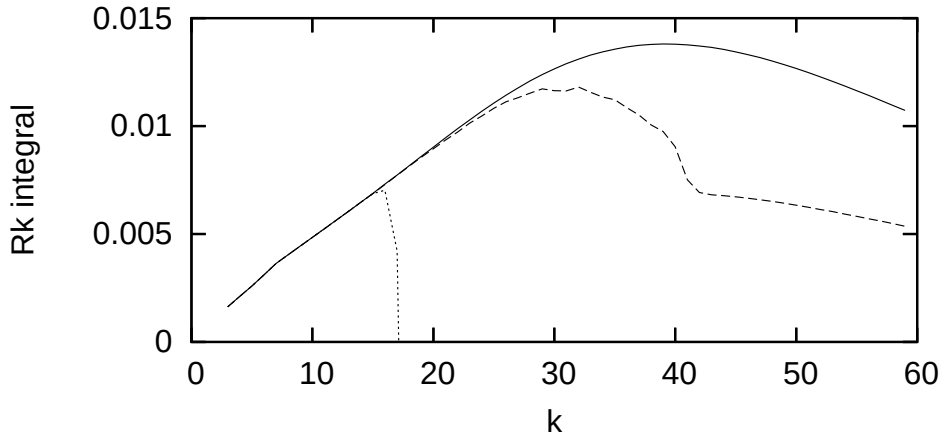

Figure 1: A representative R_k continuum-countinuum exchange integral evaluated in the standard R-matrix codes: —, full exchange; - - -, semi-exchange (as in DARC); ....., exchange cut-off due to onset of erratic behaviour (RMATRX1).

forward integration, which is not stable for large k in the second integral of (4). This is because r^{-k-1} is large when r is small, and even though orbitals tend to zero at $r = 0$, their non-zero behaviour near the origin will be blown up by r^{-k-1} if k is big enough. The codes have different strategies for dealing with the problem: in RMATRX1 a cut-off is introduced in k to zeroize the exchange integral at the onset of erratic behaviour, which has the effect of going over to a no-exchange approximation for higher partial waves; in DARC, the second integral in (4) is set zero (this is not done explicitly, but is the result of making a correction to the integrals for all s based on zeroizing the integral at $s = a$). This is illustrated in figure 1 by plotting a representative R_k continuum-countinuum exchange integral from a typical R-matrix calculation, namely the He-like Fe described in section 5. The RMATRX1 cut-off appears at $k = 17$ and the DARC semi-exchange tendency (which we simulate here in RMATRX1) occurs gradually from $k = 30-40$, above which only the first integral in (4) is included.

A further problem can arise affecting mainly the first integral of (4): if the mesh near the origin is designed to represent the orbitals, it may not be sufficiently dense to represent the inverse power of r in $V(r, s)$. This can lead to errors in the integrals of (4) due to the high gradient of r^k as $r \to 0$.

3 Analytic solutions to the integration

We need an accurate benchmark for the two integrals of (4), paying particular attention to the high k problem, in order to establish reliable numerical integration methods. The following analysis is also useful in its own right, as little attention seems to have been paid to the analytical behaviour of the required integrals in

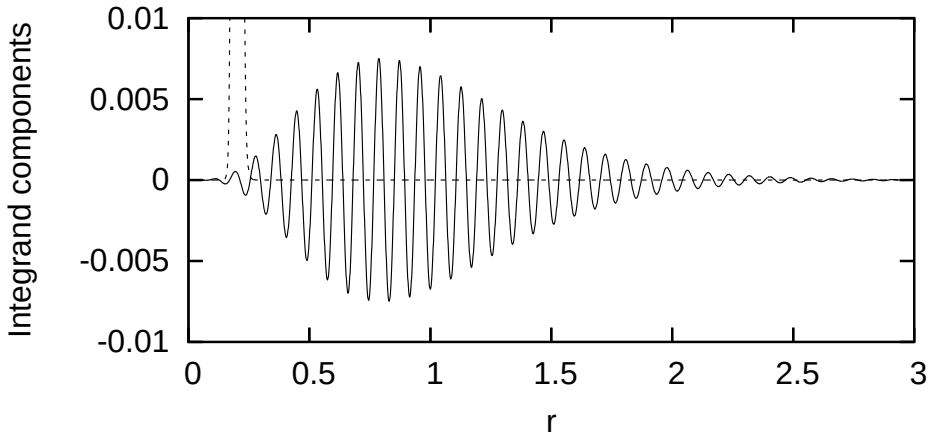

Figure 2: Components of the test integrand: —, $\exp(-\alpha r)\sin(\beta r)$; - - -, $V_{40}(r, 0.2)$.

the limit of large k in standard texts such as Gradshteyn and Ryzhik (1965).

The exchange integral involves a bound and continuum function in (4). To give a realistic but calculable approximation, we examine here a hydrogenic bound orbital of principal quantum number n and range α, $r^n \exp(-\alpha r)$, and a continuum function of wavenumber β and phase t, $\sin(\beta r + t)$.

We choose values of the parameters to give some similarity to the example case of He-like Fe considered later in section 4, namely an $n = 4$ bound orbital, an R-matrix continuum basis satisfying $U(0) = 0 = [\mathrm{d}U/\mathrm{d}r]_{r=a}$ going up to at least the 70th eigenvalue, and a scattering angular momentum of 40: so we set $n = 4$, $\alpha = 5$, $\beta = (70 + 0.5)\pi/a$, $t = 0$, $a = 3$ and $k = 40$.

To give some idea of the nature of the integrations involved in (4), we show in figure 2 the orbital product $r^n \exp(-\alpha r)\sin(\beta r + t)$. The continuum orbital is rapidly oscillating, modulated by the bound orbital which drops exponentially (so $a = 3$ suffices as the upper integration limit). The R_k integral of (3) requires evaluating (4) for all s, and for large k it can be seen that the potential $V_k(r, s)$, illustrated in the figure for $s = 0.2$ and $k = 40$, has such a high gradient $\wedge$-shaped profile that the orbitals in the region of $r = s$ are emphasised in the integrals of (4). So although the orbitals tend to zero near the origin, the potential counteracts this to some extent for small s (though eventually its $1/r$ behaviour is dominated by the orbital r^n as $r \to 0$). This leads to some interesting numerical stability considerations in the following analysis, resulting in different methods for small and large s.

In subsections 3.1 and 3.2 we solve analytically the first and second integrals of (4), and in subsection 3.3 we use these 'exact' solutions to establish accurate numerical integration methods.

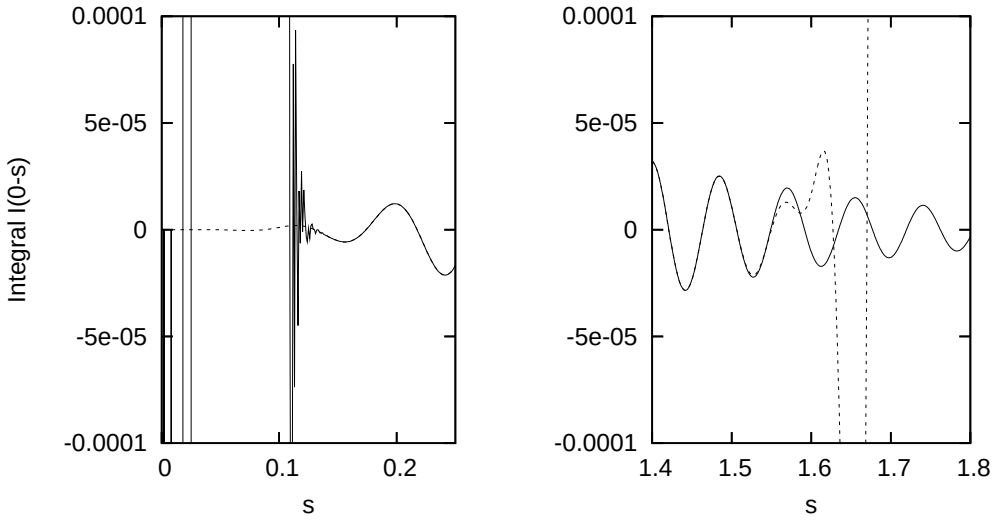

Figure 3: $I_{kn}(\alpha, \beta, s, a, t)$: —, using (6); - - -, using (8).

3.1 $I_{kn}(\alpha, \beta, s, a, t) = \int_0^s \frac{r^{k+n}}{s^{k+1}} \exp(-\alpha r) \sin(\beta r + t) \mathrm{d}r$

It is convenient to rewrite $\sin(\beta r + t)$ as complex exponentials, which are then combined with the $\exp(-\alpha r)$ term to yield an integrand of the form $r^m \exp(-zr)$ which can be integrated by standard methods (in the following z is complex, $i = \sqrt{-1}$, $0! = 1$ and $\begin{pmatrix} j \\ l \end{pmatrix}$ generates Pascal's triangle):

$$I_{kn}(\alpha, \beta, s, a, t) = \frac{i}{2s^{k+1}} \left[e^{it} K_{k+n}(\alpha + i\beta) - e^{-it} K_{k+n}(\alpha - i\beta) \right], \quad (6)$$

$$K_m(z) = \int_0^s r^m \exp(-zr) \mathrm{d}r = \frac{m!}{z^{m+1}} \left[1 - \exp(-zs) \sum_{j=0}^{m} \frac{(zs)^j}{j!} \right]. \quad (7)$$

This is accurate for large s and small m. But for $s \to 0$ or large m the summation over j in (7) becomes a close representation to $\exp(zs)$, so the square bracketed quantity can be subject to large subtraction errors as it tends to zero. This is shown in our test case in the left frame of figure 3, where the solid line (6) becomes erratic below $s = 0.15$.

In this situation, we rewrite the j summation in (7) as $\exp(zs) - \sum_{j>m} (zs)^j / j!$, and so obtain the same expression as would result from integrating $r^m \exp(-\alpha r) \sin(\beta r + t)$ by parts to raise the power of r, with $m = k + n$,

$$I_{kn}(\alpha, \beta, s, a, t) = s^n \sum_{j \geq 0} \frac{(-s)^j C_j(\alpha, \beta, s, t)}{(m + j + 1)(m + j) ... (m + 1)}, \quad (8)$$

where $C_j(\alpha,\beta,r,t)$ is the jth derivative of $\exp(-\alpha r)\sin(\beta r+t)$,

$$C_j(\alpha,\beta,r,t) = (-\alpha)^j\exp(-\alpha r)\left[\sin(\beta r+t)\sum_{l=0,2,4\ldots}^{j}\binom{j}{l}\left(\frac{\beta}{\alpha}\right)^l(-1)^{l/2}\right.$$
$$\left.+\cos(\beta r+t)\sum_{l=1,3,5\ldots}^{j}\binom{j}{l}\left(\frac{\beta}{\alpha}\right)^l(-1)^{(1+l)/2}\right]. \quad (9)$$

When $s\to 0$ and/or m is large, the $j=0$ term in (8) dominates. But as s increases, the dominant terms in (8) move to increasingly higher j, so that the summation has to be extended over a wide range of j to obtain convergence, and moreover the series has alternating signs. This can give rise to rounding errors, and is particularly serious if the terms have not declined to negligible values before the expansion has to be stopped because of computational overflow in the factorial evaluations. This is shown in our test case in the right frame of figure 3, where the dashed line (8) becomes erratic above $s=1.6$.

In practice, we find significant overlap in the range of s where both (6) and (8) are accurate, as shown in figure 3 where the continuous and dashed line are coincident between $s=0.15$ and $s=1.6$. A simple switch between the two methods therefore suffices, namely to use (8) only for the range of low s and high m where the maximum term is $j=0$ or 1.

3.2 $J_{kn}(\alpha,\beta,s,a,t)=\int_s^a \frac{s^k}{r^{k+1-n}}\exp(-\alpha r)\sin(\beta r+t)\mathrm{d}r$

For large s an efficient way to do this integral is to Taylor expand $\exp(-\alpha r)/r^{k+1-n}$ about the mid-point of the integration limits, $A=(a+s)/2$, which has the effect of converting the integrand into $\sin\beta r$ times positive powers of r which is then integrated using standard formula. In this expansion we require the jth derivative of $r^{-m}\exp(-\alpha r)$,

$$D_j(\alpha,A,m) = (-1)^j\exp(-\alpha A)\sum_{l=0}^{j}\binom{j}{l}\alpha^{j-l}A^{-m-l}\frac{(m+l-1)!}{(m-1)!} \quad (10)$$

So the required integral is, with $m=k+1-n$ and $t=0$,

$$J_{kn}(\alpha,\beta,s,a,t)=s^k\sum_{j\geq 0}D_j(\alpha,A,m)\frac{1}{j!}\int_s^a(r-A)^j\sin(\beta r+t)dr$$
$$=s^k\sum_{j\geq 0}D_j(\alpha,A,m)\sum_{l=0}^{j}\frac{1}{(j-l)!\beta^{l+1}} \quad (11)$$
$$\times[(s-A)^{j-l}\cos(\beta s+t+l\pi/2)-(a-A)^{j-l}\cos(\beta a+t+l\pi/2)].$$

For $s\to a$ this converges quickly in j. But for $s\to 0$ it is not accurate because of the large number of j terms required to obtain convergence. In order to obtain

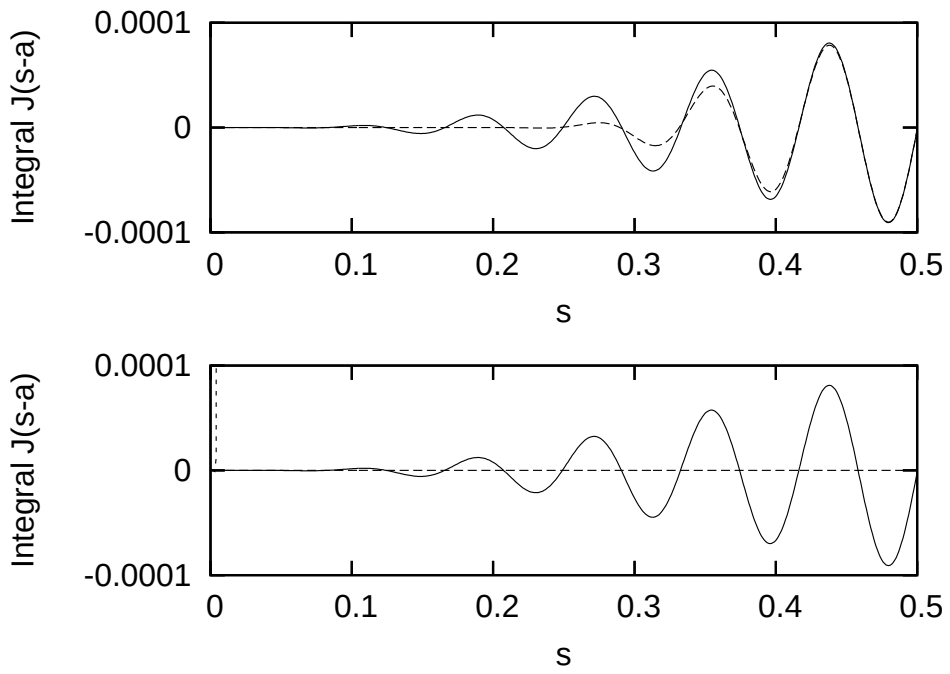

Figure 4: $J_{kn}(\alpha, \beta, s, a, t)$. Upper frame uses analytical methods: —, exact (12); – – –, (11). Lower frame uses numerical methods: —, backward integration using (13) below $s = 0.032$ defined by (16); vertical dashed line, forward integration.

the correct form for $s \to 0$ we integrate by parts j' times, to reduce the power of $1/r$, and use $C_j(\alpha, \beta, r, t)$ defined by (9),

$$J_{kn}(\alpha, \beta, s, a, t) = \sum_{l=0}^{j'} \frac{s^{n+l} C_l(\alpha, \beta, s, t) - (s/a)^k a^{n+l} C_l(\alpha, \beta, a, t)}{(k-n)...(k-n-l)} + \frac{1}{(k-n)...(k-n-j')} \int_s^a \frac{s^k}{r^{k-n-j'}} C_{j'}(\alpha, \beta, r, t). \qquad (12)$$

The right-hand integral in (12) requires two evaluations of $J_{k,k-n-j'}(\alpha, \beta, s, a, t)$ defined by (11), with t and $t+\pi/2$ corresponding to the $\sin(\beta r+t)$ and $\cos(\beta r+t)$ of (9). In practice we find (12) gives good numerical results for all s when integrating by parts a fixed small number of times (eg. $j' = 3$), that is, this technique improves the result for small s without affecting the quality of (11) for large s. The resulting exact integral in our test case is shown as a continuous line in the upper frame of figure 4, and (11) is shown as a dashed line; the two are coincident above $s = 0.4$.

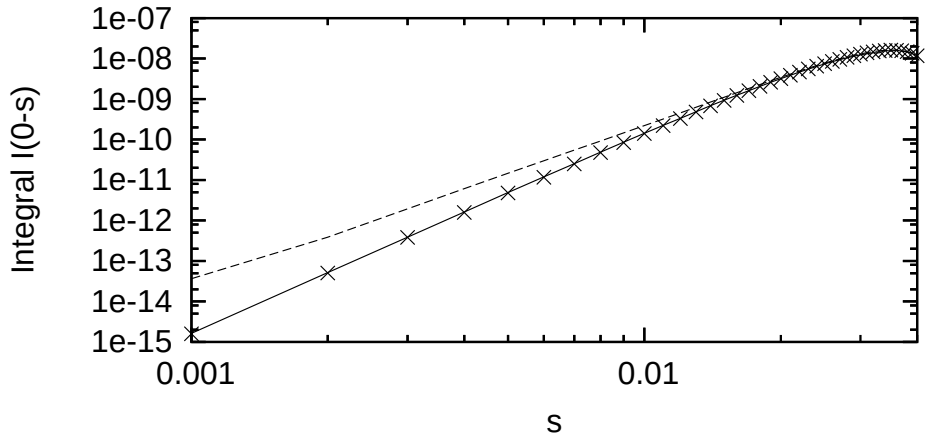

Figure 5: $I_{kn}(\alpha, \beta, s, a, t)$: —, numerical integration using (15); ×, exact from (8); - - -, Simpson's integration.

3.3 Numerical solutions to the integration

We have already discussed in section 2 that the second integral in (4) must be evaluated in a backwards direction for stability. This is shown graphically for our test case in the lower frame of figure 4, where we plot the results from forward Simpson integrations used in RMATRX1 and DARC (Berrington et al 1995; RmaX 2006; Ait-Tahar et al 1996; Norrington 2006). In both cases the result rises almost vertically from the origin towards the upper limit of floating point number representation on most computers. As stated earlier, both programs automatically throw out such results: DARC by zeroizing this particular integral, and RMATRX1 by zeroizing the whole exchange term. By contrast, backward Simpson integration, as shown by the continuous line in the lower frame of figure 4, gives stable results agreeing with the exact analytical solution in the upper frame.

We address here the final problem of section 2, namely the representation of high powers of r on the mesh near the origin, given that the orbitals are well represented. Let $U_1(r)U_3(r)$ in (4) be $f(r)$. A simple two-point formula for the integral of $r^m f(r)$, for $\pm m$, is obtained by assuming $f(r)$ is a straight line between mesh points and integrating the power of r,

$$\int_s^t r^m f(r)\mathrm{d}r \approx a_m(t,s)f(s) + a_m(s,t)f(t) \tag{13}$$

$$\text{where } a_m(r_i, r_j) = \frac{r_i^{m+2} - r_j^{m+2}(1 + (r_i - r_j)(m+2)/r_j)}{|r_j - r_i|(m+1)(m+2)}. \tag{14}$$

If the integration starts at $r = 0$ and $f(0) = 0$ then this simplifies to

$$\int_0^t r^m f(r)\mathrm{d}r \approx \frac{t^{m+1}}{m+2} f(t). \tag{15}$$

We use the above techniques close to the origin where the ratio of r^m at adjacent mesh points exceeds $R = 3$. If the mesh points are equally spaced and $t = jh$, then this implies

$$\frac{((j+1)h)^{|m|}}{(jh)^{|m|}} \approx R \quad \Rightarrow \quad j \approx 1/(R^{1/|m|} - 1), \tag{16}$$

so for the first or second integral in (4) we use (15) or (13) up to mesh point j, and then forward or backward integration for the rest of the range.

This numerical technique is shown in figure 5 to reproduce the exact low s behaviour of our $I_{kn}(\alpha, \beta, s, a, t)$ test case integral, in contrast to the Simpson integration of RMATRX1 and DARC which systematically overestimates the integral of the concave curve near the origin.

4 Application: He-like ions

By checking the numerics against the analytical methods of section 3, we can now calculate for the first time reliable exchange integrals for high partial waves. To exploit this, we use subsection 3.3 to modify the integration methods of the two R-matrix codes, the nonrelativistic and Breit-Pauli Hamiltonian RMATRX1 (Berrington et al 1995; RmaX 2006) and the Dirac Atomic R-matrix Code DARC (Ait-Tahar et al 1996; Norrington 2006).

The simplest atomic system to show spin forbidden transitions is the helium isoelectronic sequence. Most of the work reported here concerns a nonrelativistic treatment using RMATRX1, in which the one-electron bound orbitals representing the He-like terms $1snl$ are calculated with a local Thomas-Fermi potential using the atomic structure program AUTOSTRUCTURE (Badnell 1997, RmaX 2006).

The codes are run in a straightforward way as described in their write-ups. All possible two electron configurations are included in the target wavefunction (for example the expansion of the ^1S states includes $1s^2$, $1sns$, $2pnp$ etc.), and all possible three electron configurations are included in the scattering expansion. We use as many continuum functions as necessary to reach a scattering energy of three times the ionization threshold (four times in the case of the 19 state calculation). The parameters used by the calculations are summarised in table 1. Note that as the n value of the target expansion increases, so does the radius a and the number of continuum functions needed – and also the computer time. We include mass correction and Darwing terms in the Hamiltonian. Apart from a systematic shift, the target energies show good agreement with experiment in their relative positions.

In the next subsections we show the high partial wave phenomenon in a spin changing transition, $n^1S - n^3P$; then we address whether this is a pure exchange effect, by looking at the effects of channel coupling and relativity. Then we look

Table 1: Calculation parameters for He-like Fe and Li. 'NIST' refers to NIST (2006) for experimental energies for Fe XXV (the ^3P multiplet is given as a range from level $j = 0$ to $j = 2$); 'rel' is the DARC calculation; 'nonrel' are the RMATRX1 calculations. 'Target' is number of states included in each calculation; 'U basis' is number of R-matrix continuum functions per channel; a is the boundary radius. Energies are in Rydbergs relative to ground state.

	Fe XXV					Li II
Method	NIST	rel	nonrel	nonrel	nonrel	nonrel
Target		17 level	11 term	19 term	29 term	29 term
		($n \leq 3$)	($n \leq 3$)	($n \leq 4$)	($n \leq 5$)	($n \leq 5$)
U basis		55	56	65	70	90
a a.u.		1.800	1.876	2.944	4.151	50.758
$E(2^1S)$	490.09	490.53	490.56	490.55	490.55	4.4679
$E(2^3P)$	489.91-491.14	490.28-491.66	491.30	491.29	491.29	4.4892
$E(3^1S)$	578.55	579.05	579.13	579.13	579.12	5.0808
$E(3^3P)$	578.53-578.89	579.01-579.42	579.39	579.38	579.38	5.0847
$E(4^1S)$	609.41			610.01	610.01	5.2880
$E(4^3P)$	609.40-609.55			610.12	610.12	5.2890
$E(5^1S)$	623.65				624.26	5.3824
$E(5^3P)$	623.65-623.73				624.32	5.3825

at whether transitions other than $n^1S - n^3P$ are affected. We leave a detailed discussion of the mechanism to section 5.

4.1 $n^1S - n^3P$: an example of a spin changing transition

For brevity only n^1S and n^3P are quoted in table 1; the calculations of course include all spin and angular momentum states for each n, but we focus on $n^1S - n^3P$ as an example of a spin changing transition. In figure 6 we show the partial collision strengths for $n^1S - n^3P$ in the 29-term calculations of He-like Fe at 2000 Ryd and of Li at 15 Ryd. The latter is dominated by low partial waves, but for Fe XXV as n increases a significant amount of the total collision strength comes from increasingly higher partial waves, and it is this phenomenon which may not have been fully appreciated in the past which we aim to explore in more detail.

Figure 6 also justifies our need to develop accurate integration techniques for the exchange two electron R_k integral for high partial waves. Contemporary work normally uses full exchange only for low partial waves, before switching to an approximate method to complete the collision strength sum to convergence. For spin changing transitions normally a simple geometric progression is assumed, i.e. that the collision strength drops smoothly with L. Figure 7 shows how the partial sum varies with L for Fe XXV $4^1S - 4^3P$ at 2500 Ryd with exchange correctly calculated. Only a quarter of the total is accounted for if exchange is

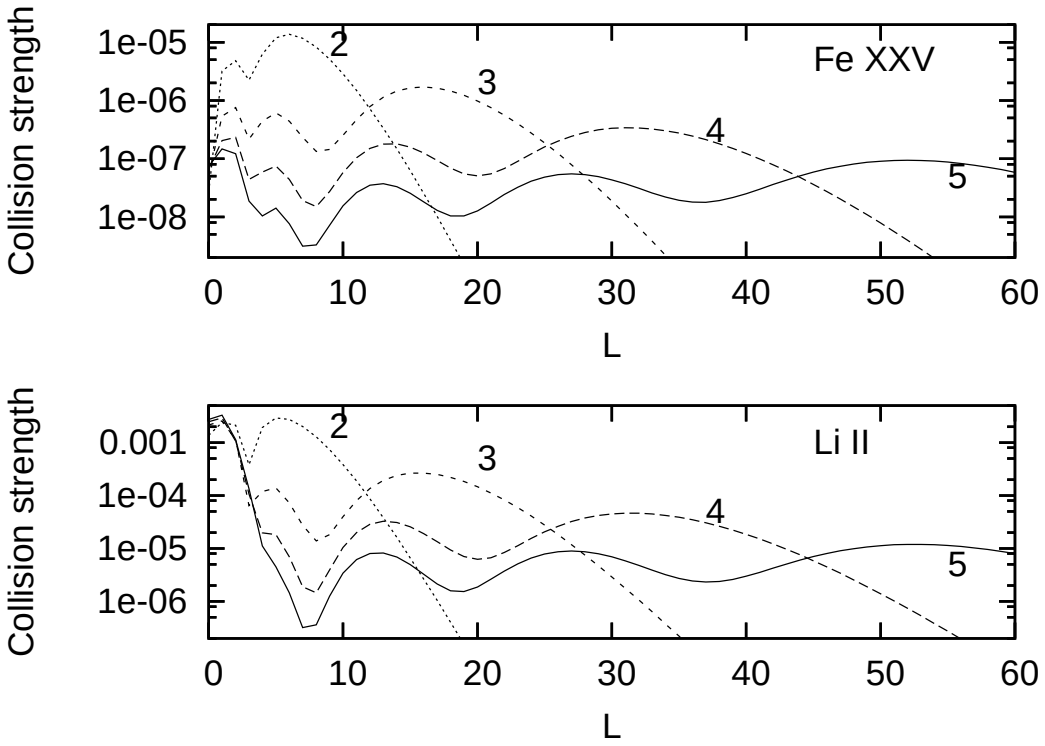

Figure 6: Partial collision strengths for $n^1S - n^3P$ in the 29-state calculations of He-like Fe at 2000 Ryd and Li at 15 Ryd. The number against each curve indicates the n value.

switched off beyond $k = 17$ (the RMATRX1 approach), and only three-quarters if the semi-exchange approach of DARC is simulated (figure 7 can be seen to be the consequence of figure 1). A geometric progression extrapolation fails spectacularly below $L = 45$, and in some cases can predict negative cross sections.

4.2 The effects of channel coupling

The coupling of nearby channels could have a profound effect on weak transitions. To investigate this we carry out a special 13-term calculation, in which we include all eleven terms with $n \leq 3$ together with 4^1S and 4^3P, omitting the nearby terms such as 4^3S and 4^1P etc. We then examine the $4^1S - 4^3P$ transition and compare with the 19 term calculation, with and without exchange above $k = 17$.

The partial collision strength comparison is shown in figure 8 for Fe XXV and Li II. At low partial waves, where channel coupling is expected to play a role, the 13 term and 19 term results disagree, more so for Li where low partial waves dominate the collision. At high partial waves the 13-term and 19-term full exchange results agree, and these waves dominate the Fe collision; the no-exchange collision strength is essentially zero, from which we conclude that the

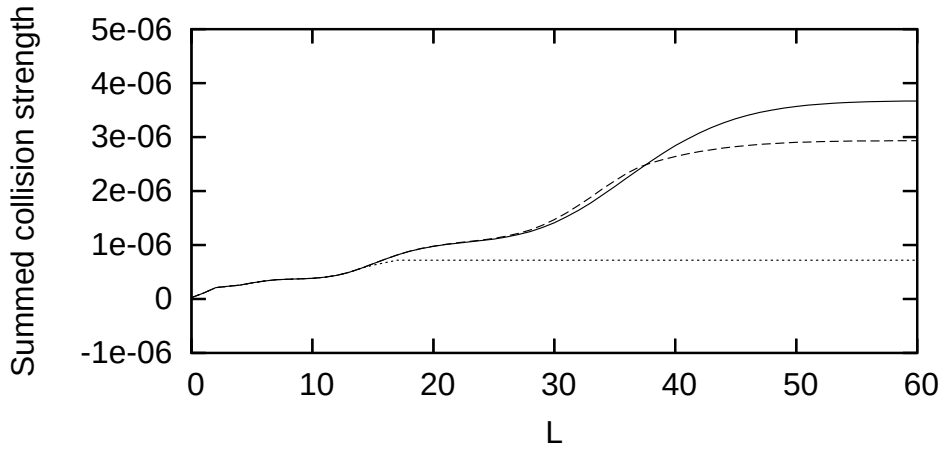

Figure 7: Collision strength summed up to the given L for He-like Fe $4^1S - 4^3P$ by 2500 Ryd electrons, in a 19 term R-matrix calculation. —, full exchange; - - - -, semi-exchange (cf. DARC); ...., no exchange beyond k=17.

mechanism here is exchange. We look at the iso-electronic trend in more detail later.

4.3 The effects of relativity

An objection could be raised that a spin changing transition may be modified by the $\mathbf{l} \cdot \mathbf{s}$ spin orbit interaction and other relativistic effects. In particular, we note in table 1 that the fine structure splitting of n^3P places the $j = 0$ level below the n^1S, and the other two levels above, so part of the $n^1S - n^3P$ transition is energetically forbidden. In addition $n^1S_0 - n^3P_1$ is dipole allowed and therefore has different dynamics to the forbidden transitions. So we now compare the RMATRX1 calculation with a relativistic one using DARC (Ait-Tahar et al 1996, Norrington 2006).

The target orbitals are produced in the Dirac-Fock formalism using the General Relativistic Atomic Structure Package GRASP (Dyall et al 1989, Parpia 1996). However, the (older) version of GRASP which is currently linked to DARC uses a logarithmic radial mesh which fails to converge highly excited orbitals, so our relativistic runs are restricted to a 17-level calculation with $n \leq 3$. In figure 9 we compare partial collision strengths for $3^1S_1 - 3^3P_2$ and $3^3P_0 - 3^1S_1$ from DARC of He-like Fe at 2000 Ryd, with the nonrelativistic $3^1S - 3^3P$. We also show the similarity of the dipole transitions $3^1S_0 - 3^3P_1$ and $3^1S - 3^1P$. Allowing for statistical factors, the agreement is excellent, particularly in the contribution coming from the higher partial waves to the forbidden transitions. Thus the exchange effect is not disturbed by relativity in this case. This confirms earlier findings that a fully relativistic treatment is not essential for Fe ions (Berrington et al 2005).

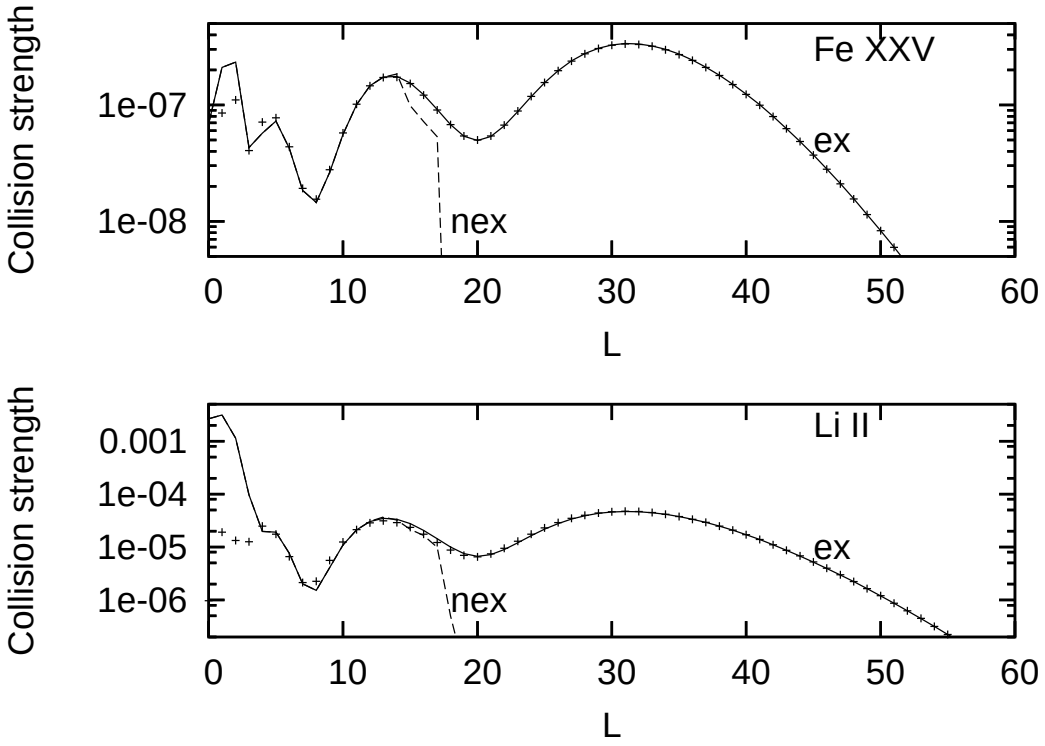

Figure 8: Partial collision strengths for $4^1S - 4^3P$ in Fe XXV at 2000 Ryd and Li II at 15 Ryd, 'ex' has full exchange; 'nex' cuts off exchange above $k = 17$: —, 19-term (ex); - - -, 19-term (nex); +++, 13-term (ex).

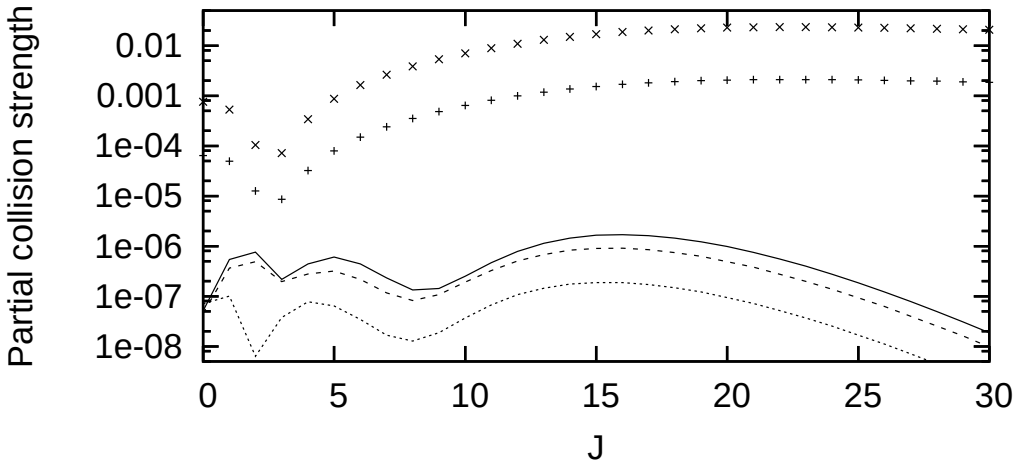

Figure 9: Comparison of nonrelativistic (RMATRX1) and relativistic (DARC) partial collision strengths for He-like Fe at 2000 Ryd. —, nonrelativistic; - - -, $3^1S_0 - 3^3P_2$; ..., $3^3P_0 - 3^1S_0$; +++, $3^1S_0 - 3^3P_1$; $\times\times\times$, $3^1S - 3^1P$.

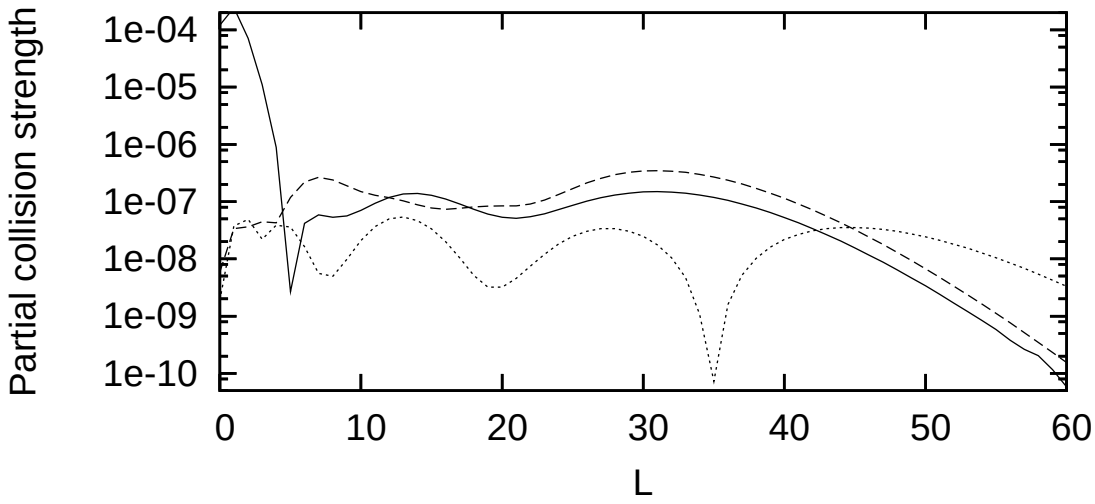

Figure 10: Partial collision strengths for He-like Fe at 2000 Ryd: —, $4^3S - 4^1S$; - - - -, $4^3S - 4^1D$; ...., $4^1S - 5^3P$.

4.4 What other transitions are involved?

Is there any significance to the near-degeneracy of the states in the transition we have chosen to examine, $n^1S - n^3P$? In figure 10 we show three other spin forbidden transitions in He-like Fe at 2000 Ryd. All show high partial wave oscillations. But for 4^3S-4^1S the low partial waves dominate anyway. The other two transitions are similar to the n^1S-n^3P cases examined, in that a significant part of the collision strength comes from high partial waves; this includes $4^1S - 5^3P$ which involves two different n shells, indicating that near-degeneracy is not necessary, though extended overlapping orbitals is important as we shall see in the next section.

Rather than showing all transitions individually here, to look for high partial wave dominance, we look at the distribution of errors arising from the exchange cut-off of RMATRX1 and the semi-exchange tendency of DARC as noted in figure 1. We show this in figure 11 for the 19-term Fe XXV calculation at 2500 Ryd, where all transitions are represented in a scatter plot of collision strength summed to $L = 60$ against the relative difference between the exact and the RMATRX1 or DARC approaches. This shows how many transitions have exchange contributions at high partial waves, and therefore the importance of an accurate evaluation of these. The RMATRX1 approach gives the greater errors, and the largest errors of both DARC and RMATRX1 are associated with $n^1S - n^3P$ (and these were shown in figure 7). There are significant differences for many transitions, but all are associated with rather small cross sections.

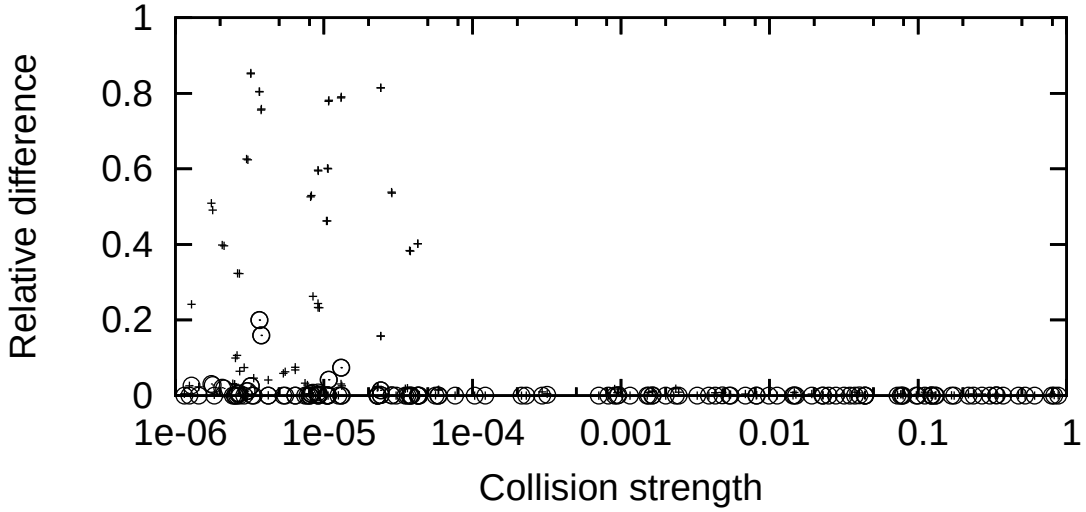

Figure 11: Errors in the calculation of collision strengths at 2500 Ryds for transitions involving all 19 terms in He-like Fe, relative to a full exchange calculation: $\odot$, semi-exchange; +, no exchange beyond k=17 (these correspond to the DARC and RMATRX1 approaches of figure 1).

5 The mechanism of the high partial wave contribution

In the top frame of figure 12 we plot the $5s$ and $5p$ radial orbitals for He-like Fe, and their shape bears some relation to the shape of the partial collision strengths for $5^1S - 5^3P$ in figure 6. It is this relationship, and the dependence on energy, that we want to explore here.

Figure 12 (top frame) also shows an example of the potential $V_k(r, s)$, and it is clear that for high k this is acting like a Dirac delta function in the R_k integral (3), so that the inner integral over r is approximately the value of the integrand at $r = s$. This indicates that for high k the exchange integral is related to the overlap of the bound orbitals. Taking the classical analogue of angular momentum as the product of linear momentum κ and radius, we can define a continuous $L = \kappa r = (E - E_i)^{1/2} r$, where E is the total energy and E_i the energy of the target state (i.e. as given in table 1). The collision strength in a pure exchange regime will be related to the square of the exchange two-electron matrix element. We therefore define the following function to compare with the collision strength profile,

$$W(L) = \frac{1}{4}(2L+1)(2S+1)\left[\int U_{nl}(r) V_L(r, L/\kappa) U_{nl'}(r) \mathrm{d}r\right]^2 \qquad (17)$$

In the bottom two frames of figure 12 we plot $W(L)$ calculated from the $5s$ and $5p$ orbitals of Fe XXV alongside the partial collision strength calculated for

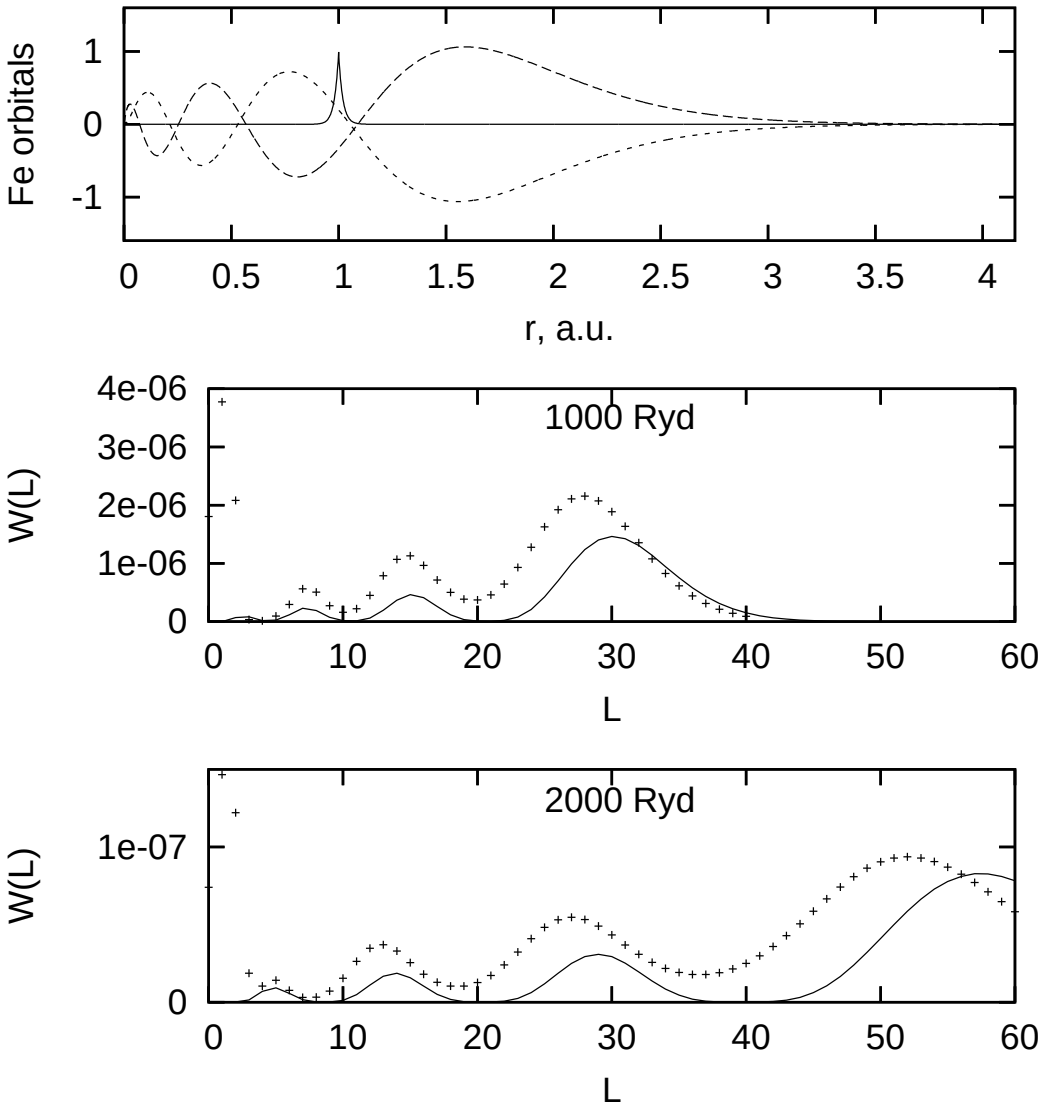

Figure 12: Top figure, radial orbitals for FeXXV: – – –, $5s$; - - -, $5p$; —, $V_{52}(r,1)$. Bottom figures, scaled W(L) at 1000 Ryd and 2000 Ryd for Fe $5^1S - 5^3P$; +++, partial collision strengths.

Table 2: Estimates of the maximum partial wave ($J_{\max}$) required to converge the collision strength sum for Fe XXV $n^1S - n^3P$ based on (18). A reference is given to the relevant figure in this paper.

n	$J_{\max}$	Energy, Ryd.
2	12	2000 (figure 9)
3	27	2000 (figure 9)
4	56	2500 (figure 7)
5	74	2000 (figure 6)

$5^1S - 5^3P$. $W(L)$ has been scaled on this plot, so there is only a proportionate relationship; there is also a small displacement in L between $W(L)$ and the collision strength. Nevertheless, the agreement with respect to both the energy and angular momentum variation is good, and justifies the view that the high partial wave contribution to this cross section is governed purely by exchange.

5.1 A summary of the findings for He-like ions

In atomic units, $r = n^2/(Z - z_{\rm screen})$ for a nuclear charge Z reduced by an electronic screening factor $z_{\rm screen}$ corresponds to the Bohr radius of the electron orbital, often used to provide an impact parameter cut off for the scattering electron. A comparison of figure 6 and 7 for the $n = 4$ case shows that one has to go significantly beyond the partial wave maxima to obtain convergence of the sum, which indicates that one needs to integrate (17) well beyond the orbital maxima shown in the top frame of figure 12. We therefore suggest doubling the Bohr radius to estimate the upper limit $J_{\max}$ of the partial wave expansion, to account for all the structure in the partial cross sections for a spin changing transition involving an excited nl electron:

$$J_{\max} \approx 2(E - E_i)^{1/2} n^2/(Z - z_{\rm screen}). \qquad (18)$$

We choose $z_{\rm screen} = 0.9$ on the grounds that the final peak in the partial collision strength shown in figure 8 at $L = 32$ is at 2000 Ryd for Fe and at 15 Ryd for Li. In table 2 we tabulate $J_{\max}$ for $n = 2$ to $n = 5$ for Fe XXV; these provide good estimates of the angular momentum range required to converge the cross sections for Fe XXV, as can be seen from the partial wave plots presented in this paper.

Figure 13 shows the isoelectronic trend of 4^1S-4^3P $L = 1$ and $L = 32$ partial collision strength at $E = E_i+2.2(Z-0.9)^2$ Ryd, which corresponds to the collision strength peak at $L = 32$. The peak becomes more important along the sequence, and dominates over low partial waves for ions above $Z = 18$. We also show that the 13 term collision strength (described in subsection 4.2) is a factor of 200 down on the 19 term calculation for Li, compared with only a factor of three for Fe, showing the lesser importance of channel coupling along the sequence.

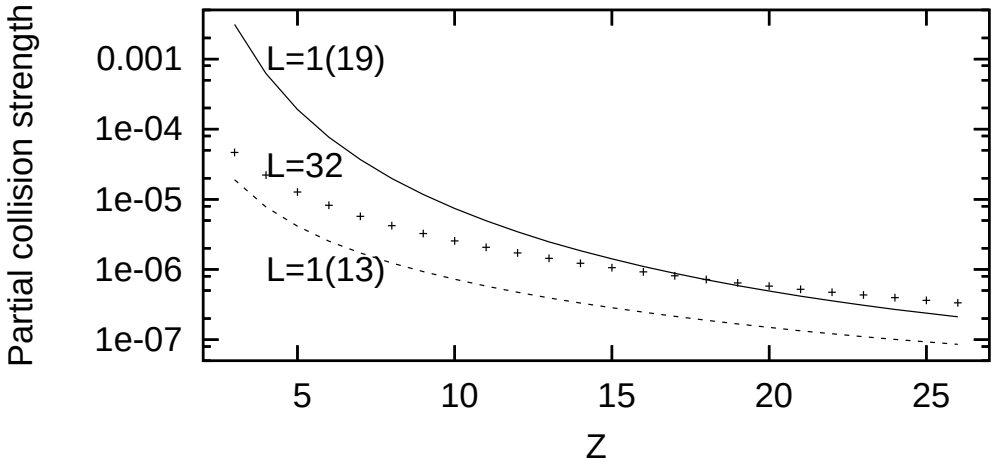

Figure 13: Isoelectronic trend of $4^1S - 4^3P$ partial collision strength at $E = E_i + 2.2(Z - 0.9)^2$ Ryd: —, L=1 (19-term); - - -, L=1 (13-term); +++, L=32.

6 Conclusion

We have examined in detail the phenomenon of high partial wave dominance in the collision strength of some spin forbidden transitions, using He-like ions as an example. This entailed benchmarking numerical integration procedures against analytic ones in order to calculate, for the first time, accurate and reliable exchange R_k integrals for high k, and to allow the widely-used R-matrix codes DARC and RMATRX1 to be modified to ensure realistic cross sections are calculated for these transitions. We have used the improved accuracy to make extensive calculations on He-like ions, to show that the spin changing transition is controlled by channel coupling in low partial waves for the near-neutral Li II, and by exchange in high partial waves for the highly ionized Fe XXV. We have checked that relativistic effects do not affect the nature of the spin-changing forbidden transitions. We have looked at the exchange mechanism, and deduced a relationship between the overlap of extended radial orbitals and the form of the collision strength at high partial waves for spin changing transitions. An estimate of the angular momentum range in which full exchange must be included to converge the collision strength is given in (18) and table 2. The large values of $J_{\max}$ suggested here may be worrying for those of us who generally ignore exchange in scattering calculations at these high angular momenta, though it should be said that the actual significance of this in practical applications may be limited by the very small cross sections of the affected transitions.

References

Ait-Tahar S, Grant I P and Norrington P H 1996 Phys. Rev. A **54** 3984

Badnell 1997 *J. Phys. B: At. Mol. Opt. Phys.* **30** 1

Berrington K A, Eissner W B and Norrington P H 1995 *Comput. Phys. Commun.* **92** 290

Berrington K A,Ballance C P, Griffin D C, Badnell N R 2005 *J. Phys. B: At. Mol. Opt. Phys.* **38** 1667–76

Burgess A, 1974 *J. Phys. B: At. Mol.Phys.* **7**, L364

Burgess A, Hummer D G, and Tully J A, 1970 Phil Trans. R. Soc. A **266**, 225

Burke P G and Berrington K A (eds.) 1993 *Atomic and molecular processes: an R-matrix approach* ISBN 0-7503-0199-6 Institute of Physics Publishing

Dyall K G, Grant I P, Johnson C T, Parpia F A, Plummer E P 1989 *Comput. Phys. Commun.* **55** 424

Fano U 1965 *Phys. Rev.* **140** A 67

Gradshteyn I S and Ryzhik I M 1965 *Tables of Integrals Series and Products* (ed. A Jeffrey) Academic Press

Hummer D G, Berrington K A, Eissner W, Pradhan A K, Saraph H E, Tully J A 1993 *Astron. Astrophys.* **279** 298

NIST 2006, http://physics.nist.gov/cgi-bin/AtData

Norrington P H 2006, http://www.am.qub.ac.uk/DARC

Parpia F A, Froese Fischer C and Grant I P 1996 *Comput. Phys. Commun.* **94** 249

RmaX 2006, http://amdpp.phys.strath.ac.uk/tamoc/code.html